

Towards a near-field concentrated solar thermophotovoltaic microsystem: Part I – Modeling

Mahmoud Elzouka, Sidy Ndao *

Mechanical and Materials Engineering Department, University of Nebraska – Lincoln, Lincoln, NE, 68588-0526, USA

Received 8 July 2014; received in revised form 15 January 2015; accepted 6 February 2015

Available online 3 March 2015

Communicated by: Associate Editor Elias K. Stefanakos

Abstract

Modeling of a near-field concentrated solar thermophotovoltaic (STPV) microsystem is carried out to investigate the use of STPV-based solid-state energy conversion as high power density MEMS power generator. Near-field radiation can be realized between two closely separated surfaces (order of radiation characteristic wavelength), resulting in the enhancement of the heat radiation flux orders of magnitudes higher than the blackbody limit, consequently increasing cell output power density. The near-field STPV model incorporates a photonic crystal absorber which transfers absorbed concentrated solar radiation to a tungsten emitter. Thermal radiation from the emitter illuminates an $\text{In}_{0.18}\text{Ga}_{0.82}\text{Sb}$ photovoltaic (PV) cell generating electrical power; waste heat is rejected from the backside of the PV cell via a microcooler. Based on the model, the near-field STPV performance is estimated for different emitter-to-PV cell separation distances d_c , emitter temperatures T_e , and emitter/absorber area ratios A_R . Results from the numerical study showed significant enhancement of the heat fluxes due to tunneling of the near-field radiation, resulting in power densities as high as 60 W/cm^2 which is 30 times higher than the equivalent far-field power density for $d_c = 20 \text{ nm}$, $T_e = 2000 \text{ K}$ and solar concentration of $\times 4350$. For a emitter/absorber area ratio of $A_R = 1$, the emitter/absorber thermal efficiency and the overall solar to electrical conversion efficiency were 73% and 15.5%, respectively. Higher power densities are achievable (up to 50 times that of far-field values) however cooling requirements and solar concentration could be a concern.

© 2015 Elsevier Ltd. All rights reserved.

Keywords: Solar thermophotovoltaic; Near-field thermal radiation; Power MEMS

1. Introduction

The world market for products incorporating micro and nanosystems is expected to exceed \$1 trillion dollars by 2020. This trend, along with global efforts to reduce our carbon footprint in favor of using renewable energy sources such as the sun, points to the need for research in small-scale, solid-state, and clean energy-based portable power generation for integrated micro/nanosystem devices such as consumer portable electronics, remote sensing

devices, unmanned aerial vehicles, autonomous robots, and BioMEMS devices. One of the most promising portable power generation alternative to batteries and micro-engines is near-field radiation transfer enabled concentrated solar thermophotovoltaic (STPV) microsystem. Unlike conventional solar photovoltaics (SPV), a concentrated STPV system converts solar radiation to electricity using heat as an intermediary through a thermally coupled absorber/emitter (Fig. 1) and has one of the highest solar-to-electricity conversion efficiency limits ($\sim 85.4\%$) while presenting opportunities for thermal storage.

* Corresponding author. Tel.: +1 402 472 1623.

E-mail address: sndao2@unl.edu (S. Ndao).

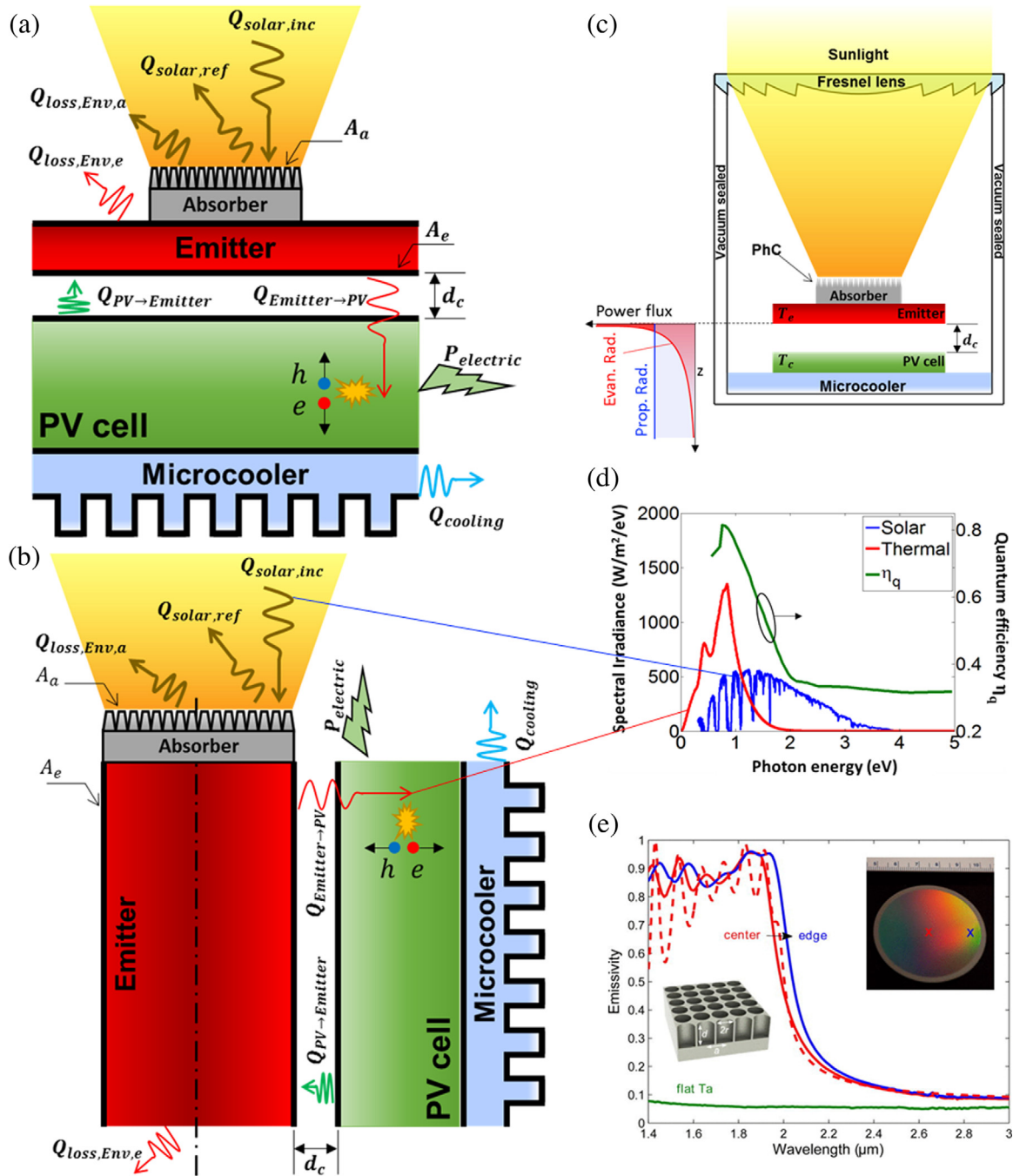


Fig. 1. Near-field STPV system layout; (a) planar arrangement and (b) cylindrical arrangement. Energy flux components are explained in nomenclature. (c) Near-field STPV system enclosure with qualitative illustration of propagating and evanescent waves' intensity as a function of distance from emitting surface. (d) Solar spectrum (AM 1.5D) and near-field radiation spectrum with the same total integrated power, both compared to the cell quantum efficiency. (e) Tantalum photonic crystal emissivity as a function of radiation wavelength (Rinnerbauer et al., 2013).

intermediate surface between the solar radiation and PV cell to modify the spectrum (Fig. 1d), hence the concept of thermophotovoltaics. STPV is also considered more flexible than conventional SPV as it can be operated with external heat source (i.e., combustion) in the absence of solar irradiance.

STPV has been investigated theoretically and experimentally; a comprehensive review of the literature

can be found in Datas (2011). Most recent efforts to improve the performance of STPVs aim to develop selective absorbers and emitters either by selecting materials with a favorable inherent selective emission (Yugami et al., 2000) or through surface nanoengineering (e.g., photonic crystals) (Lenert et al., 2014a,b; Rinnerbauer et al., 2012). In the present research, we investigate the effect of near-field thermal radiation on the performance of an

STPV; it is important to note that such study has not been performed yet in the open literature. Near-field thermal radiation transfer becomes important when the spacing (optical cavity spacing) between the emitter and the PV cells is reduced to below the characteristic wavelength of thermal radiation (unlike conventional STPV systems that generally have optical cavity spacing in the order of a few millimeters, thus limited by Planck's blackbody radiation). Thermally excited electromagnetic waves are of two types, namely, propagating waves and evanescent waves. Planck's law of blackbody radiation only accounts for propagating electromagnetic waves. On the other hand, evanescent waves are non-propagating waves that decay away from a radiating surface. However when two objects are brought close enough within a distance proportional to the nominal wavelength of thermal radiation, near-field effects due to the tunneling of evanescent waves become important, resulting in the enhancement of radiative heat transfer above Planck's blackbody limit.

Near-field radiative heat transfer has been extensively studied theoretically and recently a few experimental methods for measuring the near-field heat transfer have been proposed. Kittel et al. (2005) performed measurements of the near-field heat transfer between the tip of a thermal profiler and planar material surfaces; their results agree with theoretical calculations above 10 nm. Hu et al. (2008) reported measurements of radiative heat transfer between parallel glass surfaces separated by nanoparticles. The measured heat transfer exceeded what's predicted by Planck's blackbody law. Shen et al. (2009) measured the heat flux between a microsphere and a flat surface separated by a 30 nm gap. The corresponding heat transfer coefficients at such distance were three orders of magnitude larger than that of the blackbody radiation limit.

Near-field thermophotovoltaic (TPV) has been also investigated in the literature theoretically and experimentally (DiMatteo, 2003). Basu et al. (2009) provided a thorough review of the applications of near-field TPV devices to energy conversion, including their advantages over current technologies. A recent near-field TPV numerical model is presented in Bright et al. (2014) and Francoeur et al. (2011). Experimental work has demonstrated the feasibility of near-field TPV with reported 10x increase in power density and 30–35% fractional increase in conversion efficiency based on a 0.55 eV InGaAs diode (DiMatteo, 2003).

In the present study, numerical modeling of a near-field concentrated solar thermophotovoltaic (STPV) system is presented. Model layout is illustrated in Fig. 1c, solar radiation is concentrated via Fresnel lens and collected by a 2D tantalum photonic crystal absorber. From the absorber, heat is conducted to a tungsten emitter which reradiates the absorbed solar radiation as thermal radiation with a spectrum matching closely the PV cell's quantum efficiency (illustrated in Fig. 1d). To eliminate convection losses and prevent oxidation of the high temperature emitter and absorber, the STPV system is placed in an enclosure under vacuum. The emitter and PV cell

are brought very close to each other (separation distance is in the same order as the radiation characteristic wavelength) to explore the effects of near-field radiation. The numerical model consists of three interdependent parts: modeling of near-field thermal radiation to estimate the power transfer from the emitter to the PV cell; modeling of the absorber/emitter to estimate the net energy absorbed from the incident solar irradiance; and modeling of the PV cell to determine the photocurrent generated and cooling requirement corresponding to absorbed near-field thermal radiation from the emitter.

2. Theory

2.1. Near-field thermal radiation

Thermal radiation is customarily treated as a surface phenomenon which is analyzed using surface emissivity (Howell et al., 2010). This approach is quite acceptable when the problem characteristic dimension is much larger than radiation dominating wavelength. But when this condition is violated, the origin of radiation as a bulk phenomenon should be considered. Thermal radiation is inherent in bulk of all kind of materials; it results from the field generated due to the chaotic motion of charges within a material. This can be considered as small dipoles with random amplitudes and directions (Basu et al., 2009). The spacing effect on the net heat transfer arises from two effects that are interrelated (Basu et al., 2009). The first is wave interference due to multiple reflections inside the separation distance d_c that is important when it is close to but greater than λ_T . The second is due to photon tunneling that contributes significantly to near-field energy transfer when $d_c < \lambda_T$, which results from total internal reflection (Zhang, 2007). To investigate radiation as a bulk phenomenon, radiation should be dealt with as electromagnetic wave via the fluctuation–dissipation theorem. According to the fluctuation–dissipation theorem, thermal emission is originated from the fluctuating currents induced by the random thermal motion of charges, known as thermally induced dipoles (Rytov et al., 1989). This current induces electromagnetic waves which can be estimated via stochastic Maxwell equations. The fluctuation electrodynamics combines the fluctuation–dissipation theorem with stochastic Maxwell's equations to fully describe the emission, propagation, and absorption of thermal radiation in both the near and far field (Rytov et al., 1989). The random thermal fluctuations produce a spatial- and time-dependent electric current density $\mathbf{J}(\mathbf{x}, t)$ inside the medium whose time average is zero (otherwise any hot body will experience net electric current).

The most common technique adopted in near-field thermal radiation calculations is to express the fields in terms of dyadic Green's functions (DGFs). Using the method of potentials (Francoeur and Pinar Mengüç, 2008; Narayanaswamy and Chen, 2005), the electric and magnetic fields can be expressed as

$$\mathbf{E}(\mathbf{r}, \omega) = i\omega\mu_v \int_V V' \bar{\mathbf{G}}^E(\mathbf{r}, \mathbf{r}', \omega) \cdot \mathbf{J}^r(\mathbf{r}', \omega), \quad (1)$$

$$\mathbf{H}(\mathbf{r}, \omega) = \int_V V' \bar{\mathbf{G}}^H(\mathbf{r}, \mathbf{r}', \omega) \cdot \mathbf{J}^r(\mathbf{r}', \omega). \quad (2)$$

The ensemble average of the fluctuating current densities corresponding to emitter temperature T can be estimated by fluctuation–dissipation theorem (Rytov et al., 1989)

$$\mathbf{J}_\alpha^r(\mathbf{r}', \omega) \mathbf{J}_\beta^{r*}(\mathbf{r}'', \omega') = \frac{\omega \varepsilon_v \varepsilon_r''(\omega)}{\pi} \Theta(\omega, T) \delta(\mathbf{r}' - \mathbf{r}'') \delta(\omega - \omega') \delta_{\alpha\beta}, \quad (3)$$

where $\Theta(\omega, T)$ is the mean energy of Planck's oscillator

$$\Theta(\omega, T) = \frac{\hbar\omega}{\exp(\hbar\omega/k_b T) - 1}, \quad (4)$$

subscripts α and β indicate the two different directions of thermally induced current, $\delta(\mathbf{r}' - \mathbf{r}'')$ represents the assumption that fluctuations at two different points are correlated in the limit $\mathbf{r}'' \rightarrow \mathbf{r}'$, $\delta(\omega - \omega')$ indicates that spectral components of fluctuation currents are uncorrelated, and $\delta_{\alpha\beta}$ accounts for the assumption of isotropic media. Energy flux associated with the electromagnetic wave propagation can be estimated from the Poynting vector (Chen, 2005)

$$\langle \mathbf{S}(\mathbf{r}, \omega) \rangle = 4 * \frac{1}{2} * \text{Re} \{ \langle \mathbf{E}(\mathbf{r}, \omega) \times \mathbf{H}^*(\mathbf{r}, \omega) \rangle \}. \quad (5)$$

This expression of the Poynting vector is four times larger than its customary definition since only the positive frequencies are considered in the Fourier decomposition of the time-dependent fields into frequency-dependent quantities (Zhang, 2007). Substitution of Eqs. (1)–(3) into Eq. (5), carrying out the analytic integration along the source volume, and considering the z-component of Poynting vector (due to azimuthal symmetry), we get an expression for the near-field radiation flux from a semi-infinite body (Francoeur, 2010)

$$q_{1 \rightarrow 2}(z_c, \omega) = \frac{k_v^2 \Theta(\omega, T)}{2\pi^2} \text{Re} \left\{ i\varepsilon_{r,1}''(\omega) \int_0^\infty \frac{k_\rho}{k_{z,1}} \begin{bmatrix} g_{1 \rightarrow 2, \rho\rho}^E(k_\rho, z_c, \omega) g_{1 \rightarrow 2, \theta\rho}^{H*}(k_\rho, z_c, \omega) \\ + g_{1 \rightarrow 2, \rho z}^E(k_\rho, z_c, \omega) g_{1 \rightarrow 2, \theta z}^{H*}(k_\rho, z_c, \omega) \\ - g_{1 \rightarrow 2, \theta\theta}^E(k_\rho, z_c, \omega) g_{1 \rightarrow 2, \rho\theta}^{H*}(k_\rho, z_c, \omega) \end{bmatrix} dk_\rho \right\}, \quad (6)$$

where $q_{1 \rightarrow 2}(z_c, \omega)$ is the monochromatic radiative heat flux calculated at location $z = z_c$ and measured from the emitting surface along the z-direction in the receiver (body 2) and g are the components of dyadic green function.

In the present near-field STPV model, near-field thermal radiation was estimated between the emitter (Tungsten) and the PV cell ($\text{In}_{1-x}\text{Ga}_x\text{Sb}$). Tungsten dielectric constant

is adopted from Palik (1991), while $\text{In}_{1-x}\text{Ga}_x\text{Sb}$ is used for the PV cell. The dielectric constant of $\text{In}_{1-x}\text{Ga}_x\text{Sb}$ was calculated using the dielectric constant for GaSb and InSb combined with Vegard's law,

$$\varepsilon_{\text{alloy}}(x) = x\varepsilon_{\text{GaSb}} + (1-x)\varepsilon_{\text{InSb}} - x(1-x)C_B, \quad (7)$$

where C_B is the Bowing constant that accounts for deviations from the linear interpolation due to lattice disorders (Gonzalez-Cuevas et al., 2007). For the present study, the Bowing constant is omitted. Dielectric constants of InSb and GaSb are taken from Adachi (1999).

2.2. Photovoltaic cell

The purpose of modeling PV cell is to find out the output photocurrent corresponding to the local thermal radiation absorption. It is found from theoretical and semi-empirical modeling that for an STPV illuminated with black body at temperatures 1500–1800 °C, the optimum range for PV cell band-gap energy is 0.4–0.6 eV (Luque and Viacheslav, 2007). For this study, $\text{In}_{0.18}\text{Ga}_{0.82}\text{Sb}$ composition is used and has a band-gap energy of 0.56 eV (Park et al., 2008).

Current generated as a response of cell illumination can be estimated once the minority carrier concentration distribution is known, this is done by solving the excess minority carrier steady state diffusion equation (i.e., electrons in p-doped sides and holes in the n-doped side) (Refaat, 2006)

$$D_e \frac{\partial^2 \Delta n(z, \omega)}{\partial z^2} + G(z, \omega) - \frac{\Delta n(z, \omega)}{\tau_n} = 0, \quad (8)$$

$$D_h \frac{\partial^2 \Delta p(z, \omega)}{\partial z^2} + G(z, \omega) - \frac{\Delta p(z, \omega)}{\tau_h} = 0, \quad (9)$$

which is valid for low injection conditions and no external voltage. The term $D \frac{\partial^2 \Delta}{\partial z^2}$ is the carrier conservation term, $G(z, \omega)$ is the local generation rate of carriers (i.e., source term) and $\frac{\Delta}{\tau}$ is the recombination rate of excess minority carriers (i.e., sink term). Estimation of minority carrier diffusion coefficients $D_{e,h}$ is done by relating them to the carrier mobility $\mu_{e,h}$ via Einstein's relation

$$D_{e,h} = \frac{\mu_{e,h} k_b T_c}{e}. \quad (10)$$

The mobility of $\text{In}_{1-x}\text{Ga}_x\text{Sb}$ was calculated from Vegard's law (Eq. (7)) with the InSb and GaSb mobility values calculated from Refaat (2006). The diffusion coefficient for minority holes is estimated at $D_h = 18.3 \text{ cm}^2/\text{s}$

and for minority electrons at $D_e = 35.18 \text{ cm}^2/\text{s}$. The generation rate of electron hole pairs is given by [Bright et al. \(2014\)](#):

$$G(z, \omega) = -\frac{1}{\hbar\omega} \frac{\partial q(z, \omega)}{\partial z}, \quad (11)$$

where $\frac{\partial q(z, \omega)}{\partial z}$ represents radiation power absorbed per unit volume surrounding an element sliced at depth z . The minority carrier lifetime, τ , has three components corresponding to the recombination mechanisms: non-radiative SRH recombination, non-radiative Auger recombination, and radiative recombination. For $\text{In}_{0.18}\text{Ga}_{0.82}\text{Sb}$ at 300 K, the total minority carrier lifetimes of electrons and holes are 5.5 ns and 30.3 ns respectively ([Francoeur, 2010](#)).

The minority carrier diffusion equation is solved outside of the depletion region for p-doped and n-doped regions separately with the following boundary conditions for p-doped and n-doped regions ([Francoeur, 2010](#)) (refer to [Fig. 2](#)):

$$\Delta n(z_{dp,p}, \omega) = 0, D_e \frac{\partial \Delta n(z, \omega)}{\partial z} \Big|_{z=z_1} = S_e \Delta n, \quad (12)$$

$$\Delta p(z_{dp,n}, \omega) = 0, D_h \frac{\partial \Delta p(z, \omega)}{\partial z} \Big|_{z=z_2} = -S_h \Delta p, \quad (13)$$

where S_e and S_h are surface recombination velocities for the minority electron and hole respectively. For this

simulation, it is assumed that $S_e = 2 \times 10^4 \text{ m/s}$ and $S_h = 0$ ([Francoeur, 2010](#)).

The depletion region thickness for the p-doped and n-doped regions are calculated from [Streetman and Banerjee \(2006\)](#):

$$L_{dp,p} = \left(\frac{2\epsilon_s V_0}{e} \left(\frac{N_d}{N_a(N_a + N_d)} \right) \right)^{0.5}, \quad (14)$$

$$L_{dp,n} = \left(\frac{2\epsilon_s V_0}{e} \left(\frac{N_a}{N_d(N_a + N_d)} \right) \right)^{0.5}, \quad (15)$$

where V_0 is the p–n junction equilibrium built-in voltage and can be estimated from

$$V_0 = \frac{k_b T_c}{e} \ln \left(\frac{N_a N_d}{N_i^2} \right), \quad (16)$$

where T_c is the PV cell temperature (assumed to be constant at 300 K) and ϵ_s is the static relative permittivity calculated by [Refaat \(2006\)](#)

$$\epsilon_s = (16.8 - 1.1x)\epsilon_v. \quad (17)$$

Solving the excess minority carriers diffusion equation results in the generated photocurrent which has three components: the current from minority electrons in p-doped region, the current from minority holes in n-doped region, and the current from electron hole pairs generated within

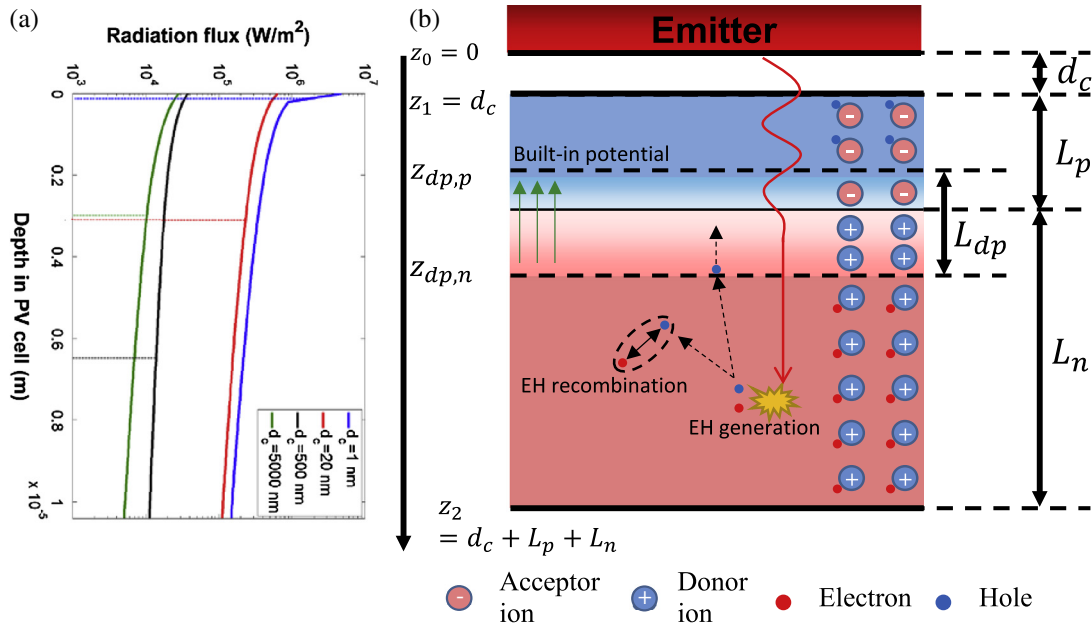


Fig. 2. Near-field TPV cell schematic; (a) near-field thermal radiation flux through the PV cell depth, dotted horizontal line represents radiation penetration depth. (b) TPV cell composed of thermal emitter illuminating a PV cell. The p-doped region of the PV cell (the upper half) has thickness $L_p = 0.4 \mu\text{m}$ and dopant concentration 10^{19} cm^{-3} , while the n-doped region has thickness $L_n = 10 \mu\text{m}$ and dopant concentration 10^{17} cm^{-3} . The emitter is the solid body above the PV cell at distance d_c from the cell. The PV cell graphic shows electron–hole generation in the n-doped region, the hole (minority carrier) generated moves towards the depletion layer by diffusion and has two possibilities; to reach the depletion region and cross to the p-doped region where it becomes a majority carrier and experience negligible recombination while contributing in electric current, or to recombine before reaching the depletion region with an electron in the n-doped region.

the depletion region (where recombination is neglected). These currents can be calculated respectively using (Francoeur, 2010)

$$J_{ph,e}(\omega) = -eD_e \frac{\partial \Delta n}{\partial z} \Big|_{z_{dp,p}}, \quad (18)$$

$$J_{ph,h}(\omega) = eD_h \frac{\partial \Delta p}{\partial z} \Big|_{z_{dp,n}}, \quad (19)$$

$$J_{ph,depletion}(\omega) = \int_{z_{dp,p}}^{z_{dp,n}} eG(z, \omega) dz. \quad (20)$$

The total photocurrent generated can be therefore determined by adding the individual photocurrents

$$J_{ph} = \int_{\omega_g}^{\infty} (J_{ph,e}(\omega) + J_{ph,h}(\omega) + J_{ph,depletion}(\omega)) d\omega, \quad (21)$$

where ω_g is the photon frequency corresponding to the PV cell band-gap energy E_g . The actual output current is the difference between the photogenerated current and the dark current (current generated when the cell is in dark condition – no electron–hole generation). The dark current can be calculated by solving the minority carrier diffusion equation in dark conditions (no electron–hole generation) (Vaillon et al., 2006). Boundary conditions are the same as in the illuminated conditions except for the concentration of minority carriers on edges of depletion region which are given by:

$$p(z_{dp,n}) = p_0 \exp(eV_f / k_b T_{cell}), \quad (22)$$

$$n(z_{dp,p}) = n_0 \exp(eV_f / k_b T_{cell}), \quad (23)$$

where p_0 and n_0 are the equilibrium hole and electron concentrations respectively. The calculated dark current is a function of voltage only and therefore independent of radiation frequency (Vaillon et al., 2006). Actual output current with respect to forward bias voltage is:

$$J(V_f) = J_{ph} - J_0(V_f). \quad (24)$$

The cell performance is assessed by the photocurrent generated, the maximum power density ($P_m = \max(V_f * J(V_f))$), and the cell conversion efficiency:

$$\eta_{TPV} = \frac{P_m}{Q_{Emitter \rightarrow PV}}. \quad (25)$$

The rest of radiation power absorbed by the PV cell which is not converted to electric power is converted to heat generation within the cell that should be rejected by a cooling system to keep the PV cell at room temperature (otherwise cell performance will deteriorate due to increased recombination rate by the elevated temperature). The heat rejected depends on the absorbed thermal radiation below band-gap energy (that cannot excite an electron from valence to conduction band, but causes lattice vibration) and heat rejected as a result of non-radiative

recombination of minority carriers. Heat rejected can be estimated from energy balance of the PV cell (Fig. 1a and b)

$$Q_{Emitter \rightarrow PV} = Q_{PV \rightarrow Emitter} + P_{electric} + Q_{cooling}. \quad (26)$$

2.3. Absorber/emitter

The absorber/emitter is the intermediate body between the solar irradiance and the PV cell; it absorbs the concentrated solar power from one side via a photonics crystal absorber and emits thermal radiation towards the PV cells from the other side with tailored spectrum. The purpose of the absorber/emitter is to convert the broad solar spectrum to a narrower thermal spectrum, which can match better the peak of the PV cell quantum efficiency curve.

Assuming that the STPV system is enclosed in a perfect vacuum, we only consider radiative heat transfer in solving the energy conservation equation in the absorber/emitter. The absorber absorbs portion of incident solar radiation

$$\begin{aligned} Q_{solar,abs} &= Q_{solar,inc} - Q_{solar,ref} \\ &= A_a n_{suns} \int_0^{\infty} (1 - \rho_a(\lambda)) q_{solar,inc}(\lambda) d\lambda, \end{aligned} \quad (27)$$

where n_{suns} is the solar concentration and $\rho_a(\lambda)$ is the photonic crystal spectral reflectivity. For opaque bodies, spectral emissivity is related to spectral reflectivity by $1 = \epsilon_a(\lambda) + \rho_a(\lambda)$. The absorber also loses heat to the surrounding at ambient temperature via thermal radiation, this can be calculated as

$$\begin{aligned} Q_{loss,Env,a} &= A_a \\ &\times \int_0^{\infty} \epsilon_a(\lambda) (E_b(T_{emitter}, \lambda) - E_b(T_{env}, \lambda)) d\lambda, \end{aligned} \quad (28)$$

where the temperature of the absorber/emitter is considered uniform. To decrease losses to the environment, absorber area should be decreased relative to the emitter area. The heat losses from the emitter area exposed to environment can be calculated for the planar arrangement (Fig. 1a) using the following equation:

$$\begin{aligned} Q_{loss,Env,e} &= (A_e - A_a) \\ &\times \int_0^{\infty} \epsilon_e(\lambda) (E_b(T_{emitter}, \lambda) - E_b(T_{env}, \lambda)) d\lambda, \end{aligned} \quad (29)$$

and for the cylindrical arrangement (Fig. 1b) using

$$\begin{aligned} Q_{loss,Env,e} &= A_a \\ &\times \int_0^{\infty} \epsilon_e(\lambda) (E_b(T_{emitter}, \lambda) - E_b(T_{env}, \lambda)) d\lambda. \end{aligned} \quad (30)$$

Using energy balance on the absorber and emitter together (refer to Fig. 1a and b) we get

$$Q_{solar,inc} + Q_{PV \rightarrow Emitter} = Q_{solar,ref} + Q_{loss,Env,a} + Q_{loss,Env,e} + Q_{Emitter \rightarrow PV}, \quad (31)$$

where $Q_{Emitter \rightarrow PV}$ is the net emitted power from the emitter to the PV cell (after considering reflection) and $Q_{PV \rightarrow Emitter}$ is the net emitted power from the PV cell to the emitter. Both can be calculated from near-field radiation transfer (Eq. (6)) taking into account the emitter area A_e . The only unknown in the heat balance equation (Eq. (31)) is n_{suns} ; which is the solar concentration. The thermal efficiency of the absorber/emitter is given by

$$\eta_{ae} = \frac{Q_{Emitter \rightarrow PV}}{Q_{solar,inc}}, \quad (32)$$

where $Q_{solar,inc}$ is defined as

$$Q_{solar,inc} = A_a n_{suns} * \int_0^\infty q_{solar,inc}(\lambda) d\lambda. \quad (33)$$

Tungsten is used for emitter and its temperature dependent spectral emissivity is adopted from Lassner and Schubert (1999), while the absorber is made of tantalum which surface is covered by 2D photonic crystal to maximize solar energy absorption, its emissivity is adopted from Lenert et al. (2014b).

Solving the minority carrier diffusion equation for absorbed spectral near-field thermal radiation corresponding to a given emitter temperature and separation distance, we get the near-field STPV output power density, cooling requirement, and TPV cell conversion efficiency. Upon determining near-field thermal radiation exchange between

the PV cell and the emitter, required absorbed solar radiation can be determined by applying conservation of energy for the absorber/emitter. Solar concentration can be estimated from the required absorbed solar radiation for a given area ratio, $A_R = A_e/A_a$.

3. Results and discussion

The near-field STPV system performance is evaluated using parameters listed in Table 1 for different emitter temperatures, separation distances, area ratios, and arrangements. Fig. 3a illustrates the effect of area ratio and separation distance on the absorber/emitter thermal efficiency. For both planar and cylindrical arrangements, decreasing separation distance increases the absorber/emitter thermal efficiency due to the effect of near-field radiation. This can be explained by considering a constant absorber/emitter temperature with variable separation distances. Radiation losses to the environment depend on the absorber/emitter temperature so they will stay constant, but decreasing the separation distance increases thermal radiation transfer to the PV cell, resulting in increased absorbed power from the sun. Increased solar absorption, while keeping the losses to the environment constant, increases the thermal efficiency. The thermal efficiency also increases with increasing area ratio for both the planar and the cylindrical arrangements; the result of decreasing the absorber area (which has higher radiation losses due to its high emissivity). For the planar arrangement, the maximum achievable thermal efficiency increases with decreasing separation distance, while for the cylindrical arrangement, the maximum achievable thermal efficiency is the same for all separation distances. The maximum thermal efficiency for the cylindrical arrangement occurs when the absorbed solar irradiance is equal to the thermal power transferred to the PV cell; this is because increasing the area ratio does not affect losses to environment unlike in planar arrangement. The optimum area ratio, which achieves around 95% of the thermal efficiency for an infinite area ratio, is plotted with corresponding thermal efficiency in Fig. 3b. Although increasing the area ratio increases the thermal efficiency, it has two drawbacks: the increased solar concentration which may not be practical, and the non-uniformity of the emitter temperature.

The solar concentration (shown in Fig. 4) generally increases with decrease in separation distance and increase in absorber/emitter temperature; this is due to the increased power flux from emitter to the PV cell. For an area ratio of one as shown in Fig. 4a, the cylindrical arrangement requires more solar concentration than the planar because the former's emitter bottom area is exposed to the environment and therefore loses more heat. A similar trend can be also seen in Fig. 4b for the optimum area ratio results.

Output power density and cooling requirements of the near-field STPV system are shown in Fig. 5 as a function of separation distance and absorber/emitter temperature.

Table 1
Parameters used for simulating the near-field solar thermophotovoltaic system.

<i>Absorber (tantalum photonic crystal)</i>	
Emissivity ϵ_a	Rinnerbauer et al. (2013) (Fig. 1e)
<i>Emitter (tungsten)</i>	
Emissivity ϵ_e	Lassner and Schubert (1999)
Dielectric constant	Palik (1991)
<i>Photovoltaic cell ($In_{0.18}Ga_{0.82}Sb$)</i>	
Band-gap energy E_g	0.56 eV
Donors concentration on the n-doped region N_D	10^{17} cm^{-3}
Acceptors concentration on the p-doped region N_A	10^{19} cm^{-1}
n-doped region thickness L_n	10 μm
p-doped region thickness L_p	0.4 μm
Dielectric constant of InSb	Adachi (1999)
Dielectric constant of GaSb	Adachi (1999)
Minority electrons diffusion coefficient D_e	35.18 cm^2/s
Minority holes diffusion coefficient D_h	18.3 cm^2/s
Minority electrons lifetime τ_n	5.5 ns
Minority holes lifetime τ_h	30.3 ns
Surface recombination velocities for the minority electrons S_e	$2 \times 10^4 \text{ m/s}$
Surface recombination velocities for the minority holes S_h	0 m/s

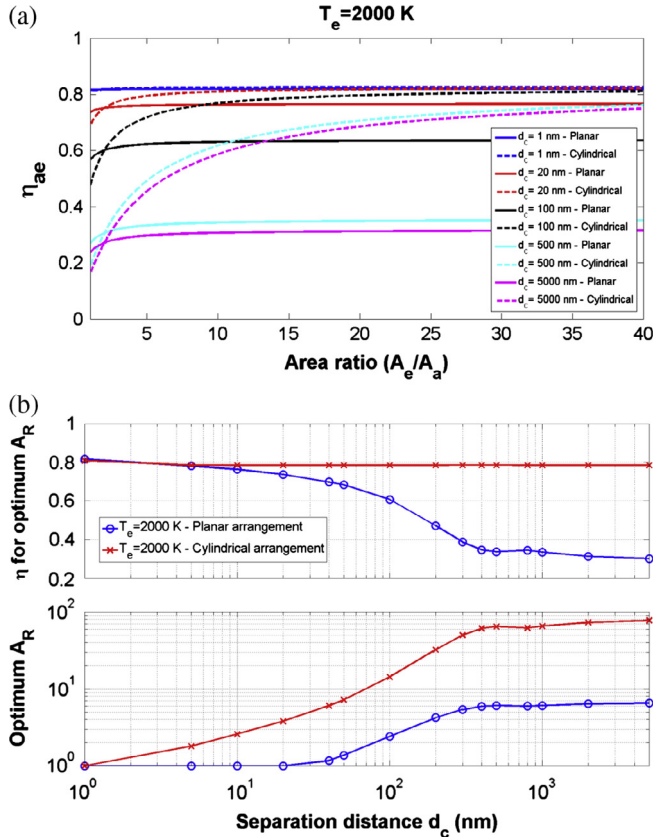


Fig. 3. Absorber/emitter performance – (a) absorber/emitter thermal efficiency versus area ratio for different separation distances and planar and cylindrical arrangements at emitter temperature = 2000 K. (b) Absorber/emitter performance at optimum area ratio for planar and cylindrical arrangements.

As predicted, the lower the separation distance and the higher the emitter temperature, the higher the power density due to the near-field radiation effects. Near-field radiation increases the power density up to 50 times higher than the far field-field value for separation distances less than 5 nm. Unfortunately this increase in power density is accompanied by increased solar concentration and increased heat rejection (i.e., cooling requirements) both of which may be design limitations. Typical solar concentration for single Fresnel lens is approximately 4600 (Luque and Viacheslav, 2007), higher concentration may be realized by complex optical system which will lead to more losses. Cooling requirements may be a design limiting factor, however significant progress has been recently realized in the thermal management of high heat-flux microsystems (Ndao et al., 2012a,b). Increased cell temperature is typical and its implications on system performance has been studied by Francoeur et al. (2011).

Conversion efficiency of near-field TPV is defined as

$$\eta_{TPV} = \frac{P_m}{Q_{Emitter \rightarrow PV}}, \quad (34)$$

and depends on the separation distance and emitter temperature (Fig. 6). As can be seen on the figure, the efficiency plot features two peaks (21.5% at 10 nm and 18% at

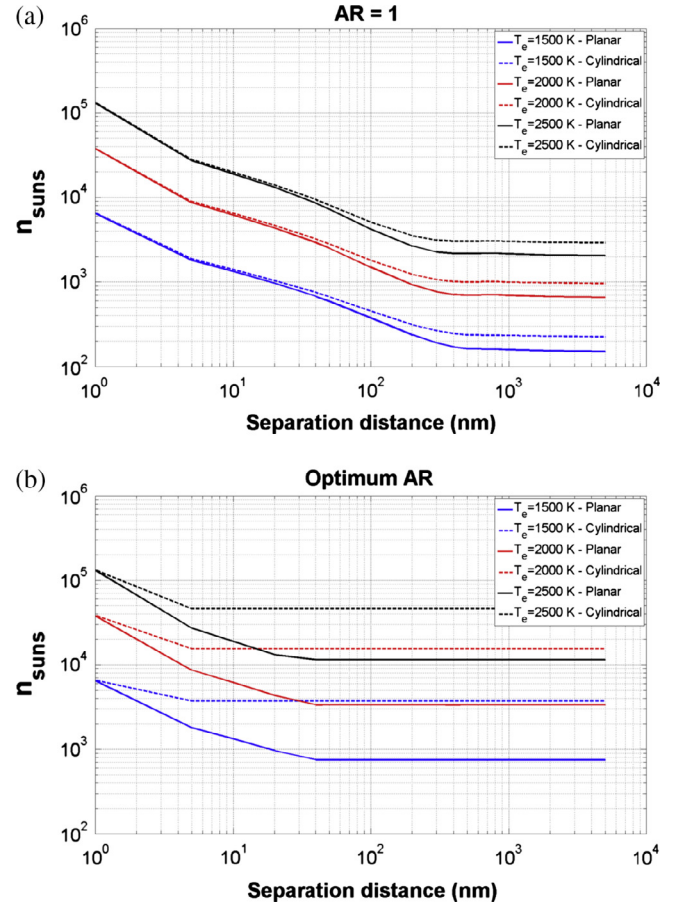


Fig. 4. Solar concentration at different absorber/emitter temperatures and planar and cylindrical arrangements – (a) for unit area ratio, (b) for optimum area ratio.

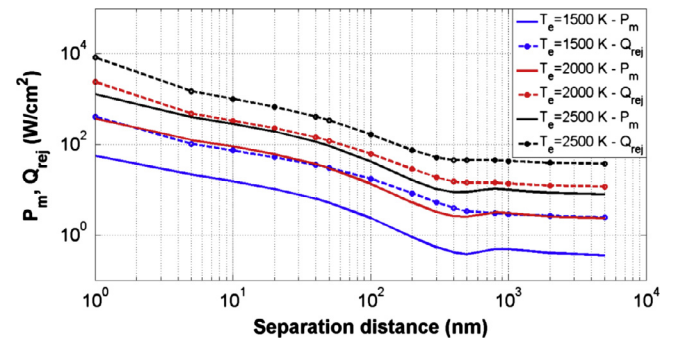


Fig. 5. Output electrical power density and rejected heat per cm² of the PV cell.

1000 nm), both of which are above the far-field efficiency (16.5%). Total efficiency of near-field STPV system is defined as

$$\eta_{STPV} = \frac{P_m}{Q_{solar,inc}} = \eta_{TPV} \eta_{ae}, \quad (35)$$

which depends on η_{TPV} , system arrangement (planar or cylindrical) and area ratio. Difference in efficiencies among different area ratios is more evident for larger separation distances (>10 nm). The highest STPV system conversion

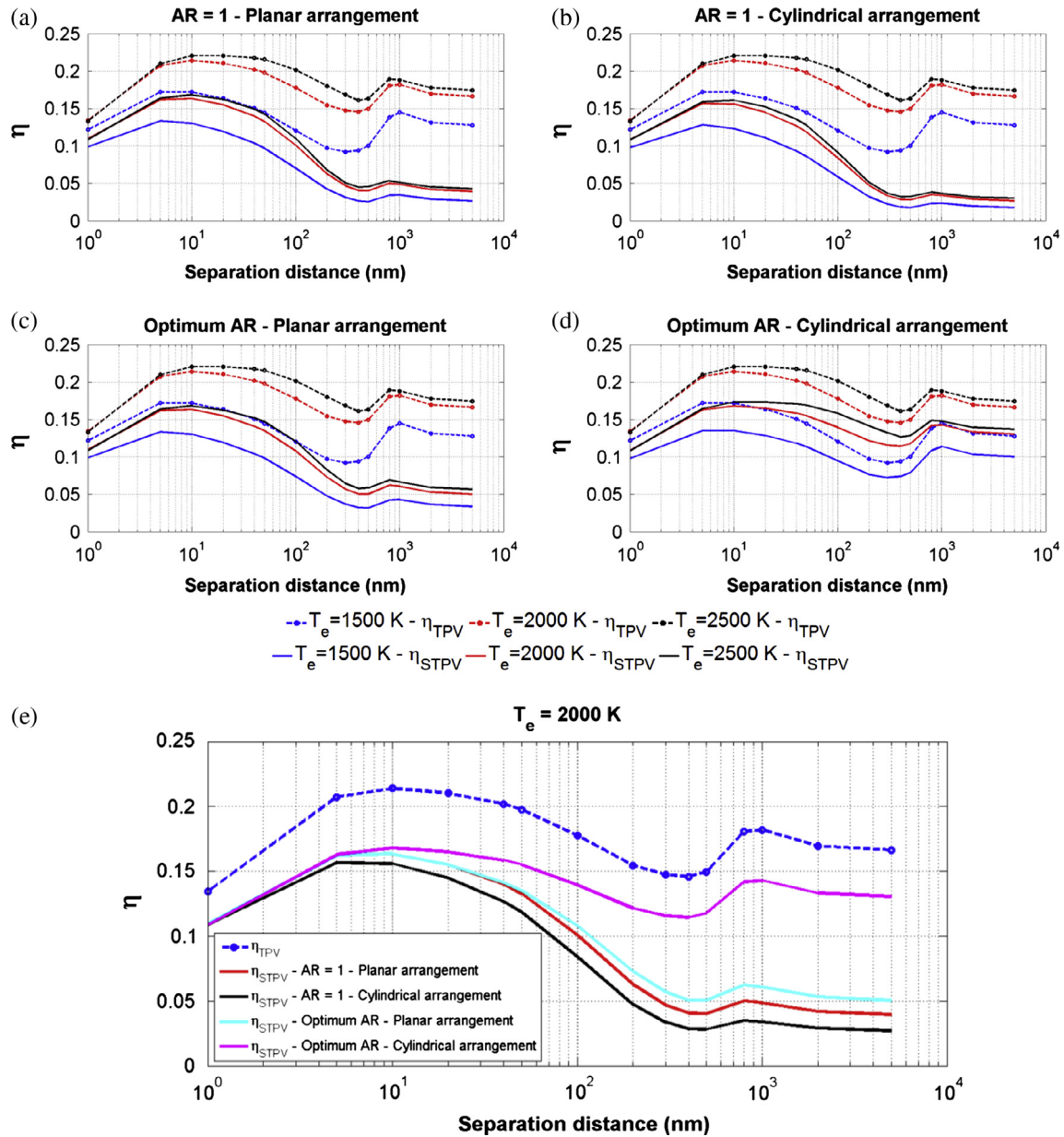


Fig. 6. TPV and STPV efficiencies at different absorber/emitter temperature and planar and cylindrical arrangements – (a) planar arrangement, unit area ratio. (b) Cylindrical arrangement, unit area ratio. (c) Planar arrangement, optimum area ratio. (d) Cylindrical arrangement, optimum area ratio. (e) Comparison between all arrangements at absorber/emitter temperature = 2000 K.

efficiencies achieved, using the cylindrical arrangement with optimum area ratio, are 16.8% at 10 nm and 14.2% at 1000 nm.

4. Conclusions

This work investigates the performance of a near-field Concentrated Solar Thermophotovoltaic (STPV) microsystem. The results revealed an increase in absorber/emitter thermal efficiency with decreasing emitter-to-PV cell separation distance. Emitter/absorber area ratio effects are found to be negligible for small separation distances (around 10 nm) however significant at relatively larger separation distances. Decreasing the separation distance increases PV

cell output power density but also increases both solar concentration and cooling requirements; therefore the minimum separation distance can be limited by solar concentration of a single Fresnel lens ($\times 4600$) or overall heat transfer coefficients of available PV cell cooling solutions. The highest achievable power density and corresponding near-field STPV conversion efficiency based on solar concentration criteria are 60 W/cm^2 and 15.5%, respectively. These were achieved at $d_e = 20 \text{ nm}$ and $T_e = 2000 \text{ K}$ using a planar arrangement. The achieved near-field STPV power density is exceptionally higher than those of high efficiency solar cells which have been reported to have maximum power densities in the order of 0.338 W/cm^2 (Green et al., 2012).

Acknowledgments

This work has been supported by a grant through the Nebraska Center for Energy Sciences Research (NCESR) with funds provided by Nebraska Public Power District (NPPD) to the University of Nebraska – Lincoln (UNL) No. 4200000844, and by funds from the Department of Mechanical and Materials Engineering and the College of Engineering at UNL, awarded to SN.

References

- Adachi, S., 1999. *Optical Constants of Crystalline and Amorphous Semiconductors: Numerical Data and Graphical Information*. Kluwer Academic Publishers, Norwell.
- Basu, S., Zhang, Z.M., Fu, C.J., 2009. Review of near-field thermal radiation and its application to energy conversion. *Int. J. Energy Res.* 33, 1203–1232. <http://dx.doi.org/10.1002/er.1607>.
- Bright, T.J., Wang, L.P., Zhang, Z.M., 2014. Performance of near-field thermophotovoltaic cells enhanced with a backside reflector. *J. Heat Transfer* 136, 062701. <http://dx.doi.org/10.1115/1.4026455>.
- Chen, G., 2005. *Nanoscale Energy Transport and Conversion: A Parallel Treatment of Electrons, Molecules, Phonons, and Photons*. Oxford University Press.
- Datas, A., 2011. *Development of Solar Thermophotovoltaic Systems*. (Dr. Diss.). Technical University of Madrid.
- DiMatteo, R.S., 2003. Micron-gap ThermoPhotoVoltaics (MTPV). In: *AIP Conference Proceedings*. AIP, pp. 232–240. doi:10.1063/1.1539379.
- Francoeur, M., 2010. Near-field radiative transfer: thermal radiation, thermophotovoltaic power generation and optical characterization. Univ. Kentucky Dr. Diss. University of Kentucky Doctoral Dissertation.
- Francoeur, M., Pinar Mengüç, M., 2008. Role of fluctuational electrodynamics in near-field radiative heat transfer. *J. Quant. Spectrosc. Radiat. Transf.* 109, 280–293. <http://dx.doi.org/10.1016/j.jqsrt.2007.08.017>.
- Francoeur, M., Vaillon, R., Mengüç, M.P., 2011. Thermal impacts on the performance of nanoscale-gap thermophotovoltaic power generators. *IEEE Trans. Energy Convers.* 26, 686–698. <http://dx.doi.org/10.1109/TEC.2011.2118212>.
- Gonzalez-Cuevas, J.A., Refaat, T.F., Abedin, M.N., Elsayed-Ali, H.E., 2007. Calculations of the temperature and alloy composition effects on the optical properties of $\text{Al}_x\text{Ga}_{(1-x)}\text{As}_y\text{Sb}_{(1-y)}$ and $\text{Ga}_x\text{In}_{(1-x)}\text{As}_y\text{Sb}_{(1-y)}$ in the spectral range 0.5–6 eV. *J. Appl. Phys.* 102, 014504. <http://dx.doi.org/10.1063/1.2751406>.
- Green, M.A., Emery, K., Hishikawa, Y., Warta, W., Dunlop, E.D., 2012. Solar cell efficiency tables (version 39). *Prog. Photovolt. Res. Appl.* 20, 12–20. <http://dx.doi.org/10.1002/ppp.2163>.
- Harder, N.-P., Wurfel, P., 2003. Theoretical limits of thermophotovoltaic solar energy conversion. *Semicond. Sci. Technol.* 18, S151–S157. <http://dx.doi.org/10.1088/0268-1242/18/5/303>.
- Howell, J.R., Siegel, R., Menguc, M.P., 2010. *Thermal Radiation Heat Transfer*, fifth ed. CRC Press.
- Hu, L., Narayanaswamy, A., Chen, X., Chen, G., 2008. Near-field thermal radiation between two closely spaced glass plates exceeding Planck's blackbody radiation law. *Appl. Phys. Lett.* 92, 133106. <http://dx.doi.org/10.1063/1.2905286>.
- Kittel, A., Müller-Hirsch, W., Parisi, J., Biehs, S.-A., Reddig, D., Holthaus, M., 2005. Near-field heat transfer in a scanning thermal microscope. *Phys. Rev. Lett.* 95, 224301. <http://dx.doi.org/10.1103/PhysRevLett.95.224301>.
- Lassner, E., Schubert, W., 1999. *Tungsten: Properties, Chemistry, Technology of the Elements, Alloys, and Chemical Compounds*. Springer Science + Business Media, New York.
- Lenert, A., Bierman, D.M., Nam, Y., Chan, W.R., Celanović, I., Soljačić, M., Wang, E.N., 2014a. A nanophotonic solar thermophotovoltaic device. *Nat. Nanotechnol.* 9, 126–130. <http://dx.doi.org/10.1038/nnano.2013.286>.
- Lenert, A., Rinnerbauer, V., Bierman, D.M., Nam, Y., Celanovic, I., Soljačić, M., Wang, E.N., 2014b. 2D Photonic-crystals for high spectral conversion efficiency in solar thermophotovoltaics. 2014 IEEE 27th International Conference on Micro Electro Mechanical Systems (MEMS). IEEE, pp. 576–579. <http://dx.doi.org/10.1109/MEMSYS.2014.6765706>.
- Luque, A.L., Viacheslav, A., 2007. *Concentrator photovoltaics*. Springer Series in Optical Sciences. Springer Berlin Heidelberg, Berlin, Heidelberg. <http://dx.doi.org/10.1007/978-3-540-68798-6>.
- Narayanaswamy, A., Chen, G., 2005. Direct computation of thermal emission from nanostructures – Begell House Digital Library. *Annu. Rev. Heat Transf.* XIV, 169–195.
- Ndao, S., Lee, H.J., Peles, Y., Jensen, M.K., 2012a. Heat transfer enhancement from micro pin fins subjected to an impinging jet. *Int. J. Heat Mass Transf.* 55, 413–421. <http://dx.doi.org/10.1016/j.ijheatmasstransfer.2011.09.037>.
- Ndao, S., Peles, Y., Jensen, M.K., 2012b. Experimental investigation of flow boiling heat transfer of jet impingement on smooth and micro structured surfaces. *Int. J. Heat Mass Transf.* 55, 5093–5101. <http://dx.doi.org/10.1016/j.ijheatmasstransfer.2012.05.009>.
- Palik, E.D., 1991. *Handbook of optical constants of solids*. *Proc. Natl. Acad. Sci. USA* 2, 87.
- Park, K., Basu, S., King, W.P., Zhang, Z.M., 2008. Performance analysis of near-field thermophotovoltaic devices considering absorption distribution. *J. Quant. Spectrosc. Radiat. Transf.* 109, 305–316. <http://dx.doi.org/10.1016/j.jqsrt.2007.08.022>.
- Refaat, T.F., 2006. Modeling of the temperature-dependent spectral response of $\text{In}_{(1-x)}\text{Ga}_x\text{Sb}$ infrared photodetector. *Opt. Eng.* 45, 044001. <http://dx.doi.org/10.1117/1.2192772>.
- Rinnerbauer, V., Ndao, S., Yeng, Y.X., Chan, W.R., Senkevich, J.J., Joannopoulos, J.D., Soljačić, M., Celanovic, I., 2012. Recent developments in high-temperature photonic crystals for energy conversion. *Energy Environ. Sci.* 5, 8815. <http://dx.doi.org/10.1039/c2ee22731b>.
- Rinnerbauer, V., Ndao, S., Xiang Yeng, Y., Senkevich, J.J., Jensen, K.F., Joannopoulos, J.D., Soljačić, M., Celanovic, I., Geil, R.D., 2013. Large-area fabrication of high aspect ratio tantalum photonic crystals for high-temperature selective emitters. *J. Vac. Sci. Technol. B Microelectron. Nanom. Struct.* 31, 011802. <http://dx.doi.org/10.1116/1.4771901>.
- Rytov, S.M., Kravtsov, Y.A., Tatarskii, V.I., 1989. *Principles of Statistical Radiophysics*. Springer-Verlag.
- Shen, S., Narayanaswamy, A., Chen, G., 2009. Surface phonon polaritons mediated energy transfer between nanoscale gaps. *Nano Lett.* 9, 2909–2913. <http://dx.doi.org/10.1021/nl901208v>.
- Shockley, W., Queisser, H.J., 1961. Detailed balance limit of efficiency of p–n junction solar cells. *J. Appl. Phys.* 32, 510. <http://dx.doi.org/10.1063/1.1736034>.
- Streetman, B.G., Banerjee, S.K., 2006. *Solid State Electronic Devices, Macromolecular Bioscience*.
- Vaillon, R., Robin, L., Muresan, C., Ménézo, C., 2006. Modeling of coupled spectral radiation, thermal and carrier transport in a silicon photovoltaic cell. *Int. J. Heat Mass Transf.* 49, 4454–4468. <http://dx.doi.org/10.1016/j.ijheatmasstransfer.2006.05.014>.
- Yugami, H., Sai, H., Nakamura, K., Nakagawa, N., Ohtsubo, H., 2000. Solar thermophotovoltaic using $\text{Al}_2\text{O}_3/\text{Er}_3/\text{Al}_2\text{O}_3$ eutectic composite selective emitter. Conference Record of the Twenty-Eighth IEEE Photovoltaic Specialists Conference – 2000 (Cat. No. 00CH37036). IEEE, pp. 1214–1217. <http://dx.doi.org/10.1109/PVSC.2000.916107>.
- Zhang, Z., 2007. *Nano/Microscale Heat Transfer*, first ed. McGraw-Hill Professional.